Journal of Materials Chemistry A

Accepted Manuscript

ROYAL SOCIETY OF CHEMISTRY

www.rsc.org/materialsA

Journal Name

RSCPublishing

ARTICLE

Electronic Interaction between Platinum Nanoparticles and Nitrogen-doped Reduced Graphene Oxide: Effect on the Oxygen Reduction Reaction

Cite this: DOI: 10.1039/x0xx00000x

Received 00th January 2012,
Accepted 00th January 2012

DOI: 10.1039/x0xx00000x

www.rsc.org/

Jiwei Ma,[a,d,†] Aurélien Habrioux,[a] Yun Luo,[a] Guadalupe Ramos-Sanchez,[b,†] Laura Calvillo,[c] Gaetano Granozzi,[c] Perla B. Balbuena,[b] and Nicolas Alonso-Vante [a,*]

In this study, low-mass loadings (*ca.* 5 wt. %) Pt/C catalysts were synthesized using the carbonyl chemical route allowing for the heterogeneous deposition of Pt nanoparticles on different carbon-based substrates. N-doped reduced graphene oxide, reduced graphene oxide, graphene oxide, graphite and Vulcan XC-72 were used for the heterogeneous deposition of Pt nanoparticles. The effect of the chemical nature of the carbon-based substrate on the Oxygen Reduction Reaction (ORR) kinetics at Pt nanoparticles surfaces was investigated. XPS results show that using N-doped reduced graphene oxide materials for the deposition of Pt nanoparticles leads to formation of Pt-N chemical bonds. This interaction between Pt and N allows for an electronic transfer from Pt to the carbon support. It is demonstrated that ca. 25% of the total amount of N atoms were bound to Pt ones. This chemical bond also revealed by the DFT analysis, induces changes in the oxygen adsorption energy at the platinum surface, engendering an enhancement of the catalyst activity towards ORR. In comparison with Vulcan XC-72, the mass activity at 0.9 V vs. RHE is 2.1 fold higher when N-doped reduced graphene oxide is used as substrate. In conjunction with the experimental results, DFT calculations describe the interaction between supported platinum clusters and oxygen where the support was modelled accordingly with the carbon-based materials used as substrate. It is demonstrated that the presence of N-species in the support although leading to a weaker O_2 adsorption, induces elongated O-O distances suggesting facilitated dissociation. Additionally, it is revealed that the strong interaction between Pt clusters and N-containing substrates leads to very slight changes of the cluster-substrate distance even when oxygen is adsorbed at the interfacial region, thus leading to a lower resistance for electron charge transfer and enabling electrochemical reactions.

1. Introduction

To address environmental and energy challenges polymer electrolyte fuel cells (PEFCs)[1, 2] represent power sources that are particularly interesting for applications in transportation and stationary power plants. For PEFCs, conventional electrocatalysts are generally based on Pt and Pt-alloy nanoparticles (NPs) supported on carbon black materials.[1, 3] Though promising fuel cell performances are currently achieved, the Pt loading is still too high for large scale applications. Two routes to decrease catalyst cost are nowadays explored: i) reducing Pt loading, and ii) exploring non-noble metal catalysts. However, it is challenging to maintain catalyst activity, especially for the oxygen reduction reaction (ORR), when the Pt catalyst loading is reduced. Moreover, it is well-known that due to their low graphitization degree, carbon black materials are unstable and electrochemically oxidize at 0.97 V *vs.* RHE, as detected by differential electrochemical mass spectrometry (DEMS).[4] Although the kinetics of the process is rather low, it is known to be responsible for reducing the cell

durability by deteriorating the electrocatalytic activity of carbon-supported Pt NPs accompanied by Pt loss and agglomeration.[5-7] Challenges associated with the use of carbon black substrates can be addressed by developing improved support materials.[5] Therefore, in the past decades, extensive investigations have been focused on exploring alternative substrates, e.g. oxide-based[5, 8-12] and graphene-like,[5, 13-23] which might induce strong and beneficial catalyst-support interactions, thereby substantially enhancing catalytic activity while decreasing Pt loading.

Graphene meets the requirements for support materials due to its large surface area, high conductivity, good chemical and electrochemical stability.[24] As a result, it has been recognized as a promising support for low-temperature fuel cell electrocatalysts.[15] Graphene-based supports are commonly prepared by reducing graphene oxide (GO) via a chemical reduction method which eventually takes to reduced GO (RGO).[15, 24] However, it is currently very challenging to control the supported-metal center morphology and dispersion. Recently, heteroatom-doped graphene materials have received much attention[24, 25] as support for electrocatalysts, paving the way for the growth of catalytically active metals with controlled morphology and dispersion on the surface of graphene support.[21, 24, 26]

In this paper, low mass loading (*ca*. 5 wt. %) Pt/C catalysts using either nitrogen-doped or undoped RGO-based materials as carbon support are prepared and electrochemically characterized with respect to ORR. Nitrogen-doped RGO (NRGO) has been intensively investigated as Pt catalyst support due to the possibility to control the composite catalyst functionality by rationalizing the high affinity between nitrogen groups and Pt atoms.[21, 26-28]

To better understand the interaction between Pt NPs and graphene-like substrates, undoped RGO was also used for comparison. Different interaction modes between Pt NPs and NRGO was identified and ascribed to charge transfer between Pt NPs and the graphene support. These interactions are related to Pt-N interactions due to the presence of nitrogen groups on the NRGO surface, as also revealed by X-ray photoemission spectroscopy (XPS) results. This study points out the effect of a support-driven electronic modification of Pt on the activity of Pt active centers towards ORR. Density Functional Theory (DFT) calculations have been performed to understand electronic modifications of Pt NPs induced by graphene-based substrates, including the effects of the extent of oxidation of graphene and the doping with nitrogen. The electrocatalytic activities of NRGO and RGO supported low mass loading Pt NPs towards ORR were significantly higher compared to a benchmarking Pt/C catalyst showing great potential for applications in PEFCs.

2. Experimental

2.1 Synthesis of GO, RGO and NRGO

GO was synthesized according to the well-known Hummers method.[29] A mixture of 3.01 g of flaked graphite (Sigma-Aldrich) and 1.50 g of $NaNO_3$ (Sigma-Aldrich, ≥99.0%) was prepared and immersed into ice. Then, 69 mL of concentrated H_2SO_4 (Normapur, 95%) was added. Thereafter, 9 g of $KMnO_4$ (Sigma-Aldrich, ≥ 99.0%) was slowly added to keep the temperature of the reaction under 20°C. After stabilization of the reaction temperature, the reaction media was heated at 35°C and stirred for 30 min. 138 mL of ultra-pure water was then slowly added, producing an exothermic effect to 98°C. Additional heating was also applied after addition of water to maintain the reaction temperature at 98°C for 15 min. The reaction was then cooled by using a water bath until stabilization of the temperature. Then the reaction media was neutralized by slowly adding 100 mL of ultra-pure water and 10 mL of H_2O_2 (VWR, 33%), producing an exothermic effect. The system was then air cooled. The reaction media was filtrated by using an 80-100 µm filter, the fine and the rough part were collected. The fractions obtained were then let to settle to remove the supernatant. They were then centrifuged at 12.000 rpm for 10 minutes and the supernatant was removed. The residues were washed two times with HCl (Normapur, 37%):H_2O, 1:3 (v/v) solution and subsequently, with ultra-pure water. The final residues were then dried at 50°C. The graphite oxide was then collected for the following experiments and characterization.

To synthesize RGO, 150 mg GO were dispersed into 100 mL ultra-pure water. The suspension was magnetically stirred for 3 h and then sonicated for 1 h. 2 mL of an 8 M NaOH solution were then added into the suspension and magnetically stirred for 30 min. Subsequently, 1.2 g of $NaBH_4$ were added and the suspension was heated at 80 °C for 1 h. The powder was recovered by centrifugation at 12.000 rpm for 10 min and washed with ultra-pure water. Finally, the sample was obtained by centrifugation at 12.000 rpm for 10 min and dried at 60 °C for 48 h. Finally, the powder was calcined at 400°C for 2 h under a reducing atmosphere (5% H_2 in N_2).

To synthesize NRGO material, 80 mg of GO were dispersed into 60 mL ethanol and magnetically stirred for 3 h. GO was exfoliated by sonication for 2 h. 2 mL water and 2 mL ammonia were then added into the solution and heated at 80°C, the mixture solution was finally transferred into a Teflon line autoclave (125 mL) and heated at 160°C for 3h.

2.2 Synthesis of Pt/C catalysts (C: graphite, Vulcan XC-72, RGO, NRGO)

Pt−carbonyl complex ($[Pt_3(CO)_6]_5^{2-}$) was synthesized through the reaction of $H_2PtCl_6 \cdot 6H_2O$ (99.95%, Alfa Aesar) and sodium acetate (anhydrous, 99%, Alfa Aesar) under a saturated CO atmosphere at ca. 55°C for 24 h. Methanol (anhydrous, 99.8%, Sigma-Aldrich) was used as solvent and the solution was stirred until the color turned into black green.[30] The molar ratio between Na^+ and $[PtCl_6]^{2-}$ was fixed to 6. After the synthesis of the Pt−carbonyl complex, NRGO, RGO, graphite and Vulcan XC-72 (Cabot, pre-annealed at 400°C under N_2 for 4h) were respectively added to the carbonyl complex solution under an inert gas atmosphere and stirred for 12 h in order to obtain ca. 5 wt. % Pt/C catalysts. The solvent was let to evaporate and the sample was rinsed with ultra-pure water. Finally, the powder was dried at 60°C overnight. The mass loading of Pt in the investigated samples was determined by thermogravimetric analysis (TGA) and was 4.6 wt. %, 4.4 wt. %, 4.1 wt. % and 4.8 wt. % for Pt/NRGO, Pt/RGO, Pt/Graphite and Pt/Vulcan catalysts, respectively.

2.3 Physical-chemical characterization

Raman spectroscopy (RS) was used to characterize the chemical status of the carbon atoms of the different supports investigated in this study. A Horiba Jobin Yvon Labram HR800UV RS spectrometer, equipped with an Ar^+ (Melles Griot) laser as illumination source and a CCD cooled detector, was used. The RS instrument was coupled to an Olympus microscope with analyzed region of 100x microscope objective.

The wavelength of the laser was 514.5 nm and the power 0.04 mW. The spectra were recorded at a resolution of 1 cm^{-1}. Simulations were performed by using Fityk software.[31]
The supported Pt catalysts were analyzed by transmission electron microscopy (TEM) (JEOL JEM-2100) operating under 200 kV.
XPS measurements were performed with a KRATOS AXIS ULTRA DLD using monochromatic Al K_α radiation (1466.6 eV, 150 W) as exciting source. The pressure during analysis was 6.0 x 10^{-8} Pa. The binding energy (BE) of the target elements (Pt 4f, N 1s and C 1s) was determined with a pass energy of 20 eV and the resolution was ca. 0.4 eV. Spectrometer energy calibration was carried out using a gold sample (Au 4f at 84 eV). The N 1s and Pt 4f photoemission lines were separated into chemical-shifted components (after Shirley background removal) using Voigt shaped peaks, imposing a FWHM in the 0.8–1.4 eV range, except for the metallic Pt component where an asymmetrical shape was used. In the case of the C 1s peak, seven different components were considered (although not all of them are present in all materials). An asymmetrical shape[32] was used for the sp^2 component, whereas symmetrical Voigt functions were used for the sp^3 component and the C-O and C-N functional groups.

2.4 Electrochemical characterization

Electrocatalytic inks of supported Pt NPs were prepared as follows: 10 mg catalysts, 250 µL Nafion® solution (5 wt. % in water/aliphatic alcohol solution, Sigma-Aldrich) and 1250 µL Milli-Q water (18.2 MΩ cm) were mixed and sonicated for 1 h. Thereafter, 3 µL of the mixture were taken and dropped on a glassy carbon electrode, previously polished with alumina 5A. Then it was dried in a stream of inert gas at room temperature for 30 min.
The electrochemical measurements were carried out in a three-electrode one-compartment cell by using a potentiostat (Autolab PGSTAT 30). The electrolyte was prepared from H_2SO_4 (99.6% Suprapur, Merck) and Milli-Q water (18.2 MΩ cm). A plate of glassy carbon and a reversible hydrogen electrode (RHE) with a Luggin capillary were used as counter and reference electrode, respectively. A rotating disk electrode (RDE) served as working electrode. The catalysts were evaluated at 25°C with cyclic voltammetry (CV) and linear sweep voltammetry (LSV) techniques, in N_2- and O_2-saturated 0.5 M H_2SO_4, for CV and ORR measurements, respectively. The samples were cycled between 0.05 and 1.2 V *vs.* RHE at a scan rate of 50 mV s^{-1}, and ORR was studied at 900 rpm using a scan rate of 5 mV s^{-1}.

2.5 DFT Models and Methods

First, a single graphene 4x4 layer was used to model the interaction between a small metallic cluster (Pt_4) with the graphenic network. The GO was modelled according to the most stable configuration reported by Lahaye et al.[33] Two oxidation degrees denoted as low oxidation graphene (LOG) and high oxidation graphene (HOG) were simulated. In both of them one side of the graphene layer is covered with hydroxyl groups while on the other only epoxy groups are present. The number of hydroxyl groups in one side of LOG is 4 and the number of epoxy groups in the other side is also 4, while for HOG there are double amount of functional groups in each side. Nitrogen was added to the graphene and GO systems in the form of pyridinic N: replacing one C atom by one N and eliminating one neighboring carbon; this structure is called G-1N. By doing so, dangling bonds naturally arise, which were eliminated by adding hydrogen atoms. To investigate the effect of a higher doping degree, two more pyridinic N sites were added (G-3N), then the interaction with the Pt_4 cluster was analyzed. The structures of the substrates are provided as supporting information (SI). Figure S1 depicts the graphene sheet, LOG, and HOG systems. In all the cases of modification of the graphene structure, atomic positions, and cell size and shape were allowed to change while for the interaction with the metallic cluster only atomic positions were allowed to change during DFT optimization.
In order to explore the effect of the cluster size on the metal/support interactions, we also report DFT calculations of Pt_{38} deposited on graphene and G-3N (3% at N). In addition, to allow more N atoms in contact with the larger cluster, we built a new graphene structure with a higher N concentration (6 % at N) that was called G-6N.
The electronic structure calculations were performed using the DFT approach with the projector augmented wave (PAW) pseudopotential for the inert core electrons and plane–wave basis set for the valence orbitals,[34, 35] as implemented in the Vienna Ab Initio Simulation Package (VASP).[36, 37] The generalized gradient approximation (GGA) in the form of the PBE exchange correlation functional was used. The plane wave basis was set up to a kinetic energy cut-off of 400 eV. The integration of the Brillouin-zone was performed using 5x5x1 Monkhorst-Pack grid[38] with Γ points included for the 4x4 graphene sheet and doped and functionalized supports while 3x3x1 for the 7x7 graphene sheet and doped systems. For DOS calculations the k-points were augmented to 9x9x1 and 5x5x1 respectively. For the partial occupancies the Methfessel-Paxton of first order with a smearing width of 0.2 was used. A conjugate-gradient algorithm is used to relax the atoms into their ground state. The convergence criteria for the electronic self-consistence loop is that the total energy change between two steps is smaller than $1x10^{-4}$ eV and $1x10^{-3}$ eV for atomic relaxation respectively.

3. Results and discussion

3.1 Physical-chemical characterization

Raman Analysis of the carbon supports. Results obtained for Vulcan, GO, RGO, NRGO and graphite supports in the spectral region of 900-1700 cm^{-1} are shown in **Figure 1**. This spectral region presents several overlapping bands. The first one, placed at *ca.* 1190-1200 cm^{-1}, is observed for all investigated carbon-based materials except for graphite support. The origin of this vibrational mode is currently not fully understood. It has been successively associated to nanocrystalline diamond,[39] hexagonal diamond[40] and sp^3 rich phase.[41, 42] The band located at *ca.* 1350 cm^{-1} corresponds to the well-known D mode. The appearance of the D-band (A_{1g} symmetry) is the consequence of the symmetry breakdown for carbon atoms located at the edge of graphite sheets.[43] The third broad band, centered at *ca.* 1500 cm^{-1}, has been associated to the presence of amorphous sp^2 phase.[44] The G-band is centered at *ca.* 1580-1590 cm^{-1}. This band (corresponding to the E_{2g} symmetry) is of particular interest since it provides information about the in-plane vibration of sp^2-bonded carbon atoms.[45] For graphite, NRGO and RGO materials, another band can be identified at *ca.* 1620 cm^{-1}. It corresponds to the D' mode. This D' mode is not identified in Vulcan and GO samples because it probably interferes strongly with the G mode that clearly complicates the interpretation of the parameters characterizing the G band (**Table 1**). The D and D' bands

are defect-induced bands. It is clearly deduced that the graphitic structure of all samples, except graphite, possesses a high degree of interstitial disorder along the c-axis between the crystallite planes.[45] This assertion is based on the observation of the intensity of the band centered at ca. 1500 cm^{-1} which essentially reaches a high intensity for RGO, NRGO, GO and Vulcan samples. In addition, the previously mentioned materials contain more sp^3 rich phases than graphite, since the intensity of their 1200 cm^{-1} band is larger.

The fitting of different spectra was performed. Lorentzian line shapes were used for D and G bands,[45, 46] whereas Gaussian ones were used to fit D' band[46, 47] as well as the bands centered at ca. 1200 cm^{-1} [45, 48] and 1500 cm^{-1}.[45] For the replication, positions of D and G bands were set by taking into account the second order Raman spectrum and particularly the positions of 2D (*ca.* 2700 cm^{-1}) and D+G (*ca.* 2940 cm^{-1}) bands (data not shown). As a result of the fit, several parameters were extracted and presented in Table 1. The I_D/I_G and $I_{D'}/I_G$ values respectively correspond to integrated intensity ratios of D to G bands and of D' to G bands.

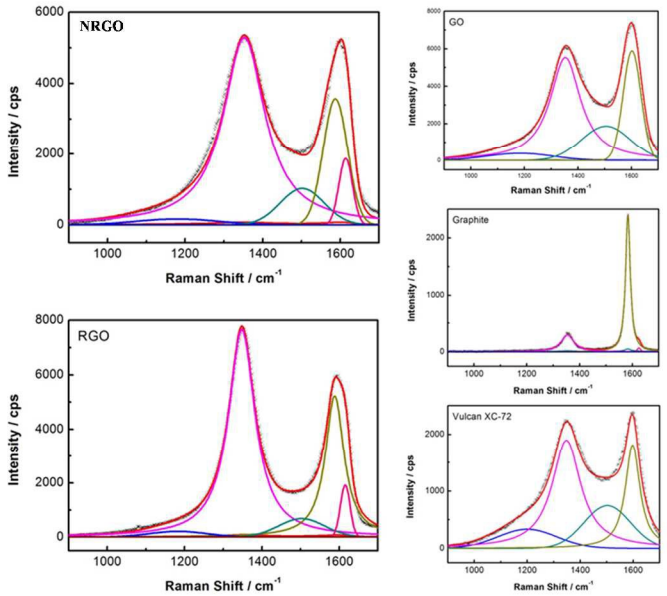

Figure 1. Raman spectra of NRGO, RGO, GO, Graphite and Vulcan substrates.

An upward shift of the G-band of all samples can be observed with respect to the position of the G-band for the graphite sample. This shift probably results from the high degree of disorder of Vulcan, GO, RGO and NRGO materials. It is in fact well-known that the G band of disordered solids is shifted to higher Raman wave numbers than the G band of ordered ones.[49] However, it can be noticed that the graphitic structure of RGO and NRGO materials is relatively more ordered than the graphitic structure of GO (G-band located at 1602 cm^{-1}), since the G-bands of RGO and NRGO are respectively located at 1588 and 1587 cm^{-1}. As the upward shift of G-band increases, it becomes difficult to separate G and D' bands. As a result, for Vulcan and GO materials, the observed band includes both G and D' ones and it can be considered that the magnitude of the shift is directly related to the percentage of contribution of D'.[50] The highly disordered character of both Vulcan and GO samples is moreover in fair agreement with the observed D and G line-widths of these two samples (Table 2). The decrease in both line widths is an evidence for the increase of the ordering degree for RGO and NRGO materials. I_D/I_G ratio allows evaluating the graphitization degree of a carbon-based material. The I_D/I_G is used as an indicator of the amount of defects in the carbon-based materials as well as to evaluate the in-plane crystallite size (L_a) which is a measure of the inter-defects distance. One of the relations describing the evolution of L_a with the integrated intensity ratio of G to D bands is the following one:[51]

$$L_a(\text{nm}) = 2.4\times10^{-10}\ \lambda_{laser}^4\ \frac{I_G}{I_D} \quad (1)$$

λ_{laser} is the laser wavelength in nm.

From the L_a values calculated for all investigated samples, it can be deduced that all samples except graphite have a low crystallite size and do not possess extended graphitic domains. Additionally the broadness of the D-band of these samples (GO, RGO, NRGO, Vulcan) can reflect a broad distribution of in-plane crystallite size. It comes as no surprise that graphite possesses larger in-plane crystallites (56.1 nm). The oxidation of graphite allowing to obtain GO is responsible for an extremely high decrease of the in-plane crystallite size (L_a value, see **Table 1**) which cannot be restored by chemical treatments leading to formation of RGO and NRGO materials. This assertion is highly supported by the evolution of L_a values from sample-to sample (**Table 1**). It can be noticed that L_a value for NRGO material (4.6 nm) is lower than L_a value for GO material (7.0 nm). This is probably due to the grafting of N-containing chemical groups at the surface of the basal planes of carbon.

Table 1. Raman parameters obtained, after curve fitting, for all investigated samples. I_D and I_G respectively correspond to D and G bands positions. $\omega_{1/2D}$ and $\omega_{1/2G}$ respectively correspond to full-width at half-maximum (FWHM) of D and G bands. L_a represents the in-plane crystallite size and is determined from Eq. 1.

	Vulcan	Graphite	GO	RGO	NRGO
ν_D (cm^{-1})	1350	1354	1353	1348	1352
$\omega_{1/2D}$ (cm^{-1})	131	30	70	41	65
ν_G (cm^{-1})	1598	1583	1602	1588	1587
$\omega_{1/2G}$ (cm^{-1})	66	10.7	39	30	37
I_D/I_G	2.1	0.3	2.4	2.1	3.7
L_a (nm)	8.0	56.1	7.0	8.0	4.6

TEM Analysis of the Pt/C catalysts. TEM images of Pt/NRGO, Pt/RGO, Pt/Graphite and Pt/Vulcan catalysts are shown in **Figure 2**. From TEM micrographs we observed that Pt NPs were highly dispersed on the NRGO and Vulcan substrates, while Pt NPs deposited onto RGO and Graphite substrates were agglomerated. The higher graphitization degree of Graphite, as revealed by Raman spectra, is probably responsible for a decrease of nucleation sites that favor the formation of large agglomerates due to a higher effective

surface energy responsible for increasing the free energy barrier.[18, 52] The mean particle sizes for Pt/NRGO and Pt/Vulcan are 2.8±1.2 nm and 2.0±1.0 nm, respectively (see **Figures 2a** and **2d**). Due to the large agglomeration degree of Pt NPs onto RGO and onto graphite, it was difficult to estimate the size of isolated Pt NPs.

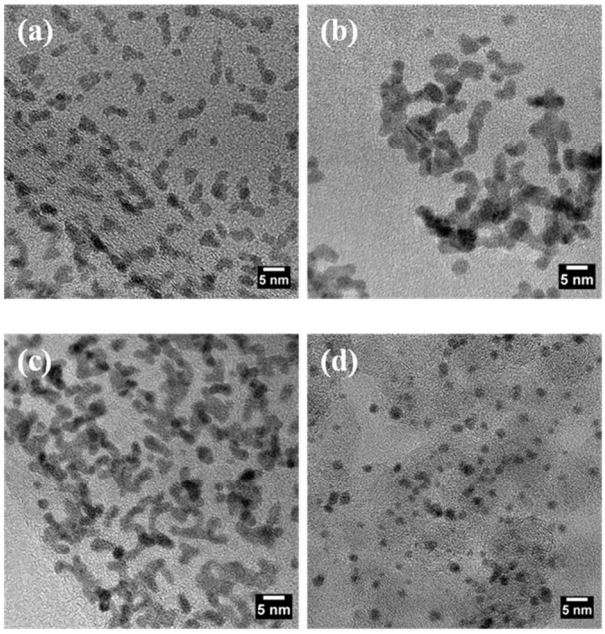

Figure 2. TEM images of Pt/NRGO (a), Pt/RGO (b), Pt/Graphite (c) and Pt/Vulcan (d) nanomaterials.

XPS Analysis of the Pt/C catalysts. In order to investigate the surface chemical status of Pt and substrate atoms in the investigated Pt/C samples, XPS measurements were carried out. The C 1s, N 1s and Pt 4f XPS data are shown in **Figure 3**, as well as the deconvolution of the experimental profiles into single chemical components. The BEs, FWHMs and relative amounts (%) of the different components in the different samples are reported in **Tables 2-4**, where the nature of each component is also briefly described. This process can furnish interesting information on the nature of the oxygen and nitrogen groups of the different carbon supports and their effect on the electronic properties of platinum.

In order to make a reliable deconvolution process, an accurate cross check of the BE and FWHM associated to each single components with literature data is needed. In this respect, we can also capitalize on the results of our previous studies on related systems (RGO[53, 54] and N-HOPG[55-57]).

Regarding the C 1s region, the main peak is always centered at 284.2 eV and it is associated to sp^2 hybridized carbon atoms (C sp^2). A minor component centered at 285.3 eV is also observed in some samples and it is associated to sp^3 hybridized carbon atoms (C sp^3). The Graphite samples (Graphite and Pt/Graphite) show also two minor components at 286.4 and 287.9 eV, attributed to tertiary alcohols and carbonyl groups, respectively, whereas the Vulcan samples (Vulcan and Pt/Vulcan) contain only a small amount of tertiary alcohols (286.3 eV). As expected, the GO sample contains a large amount of surface oxygenated groups, mainly tertiary alcohols (286.2 eV, ca. 38.8%), which are strongly reduced in samples containing RGO and NRGO. In fact, the fit of the C 1s photoemission line for NRGO confirms the presence of a graphitic sp^2 core whose basal planes are decorated by a small amount of oxygen functional groups, like tertiary alcohols (286.3 eV, ca 5%) and epoxy (287 eV, 4.2%) groups. Small amounts of carbonyl and/or carboxylic groups, which are usually decorating the edges/holes of the basal plane, are also persisting in NRGO. Finally, the deconvolution process also reveals the presence of C-N bonds (peak centered at 285.4 eV). The nature of the C-N bonds will be discussed below with the analysis of the N 1s region. Only minor changes in the C 1s composition are found when passing from the clean substrates to the corresponding Pt/C catalysts (see **Table 2**).

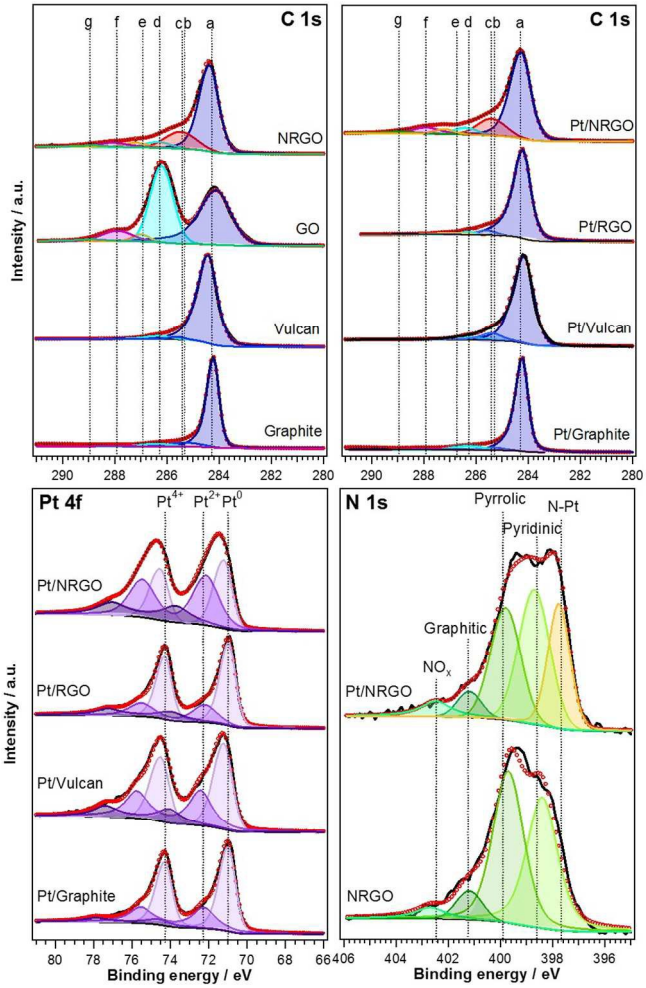

Figure 3. Deconvolution of the C 1s, Pt 4f and N 1s photoemission lines of the carbon supports and of the Pt/C catalysts into single chemical components. The raw data is represented by a solid black line, whereas the fit is represented by red cycles. Assignation of components in C 1s photoemission line: *a* C sp^2, *b* C sp^3, *c* C-N, *d* Alcohols, *e* Epoxy, *f* Carbonyl, *g* Carboxylic groups.

The N 1s photoemission line can be separated into four components centered at 398.7, 399.8, 401.2 and 402.5 eV

which are ascribed to pyridinic, pyrrolic, graphitic (substitutional), and oxidized nitrogen, respectively.[58] From the peak areas analyses (see **Table 3**), the main components of the N 1s lines are pyridinic and pyrrolic species. Pyridinic nitrogen is bonded to two carbon atoms and donates one p electron to the aromatic π system (C-N=C), whereas pyrrolic N atoms, incorporated into five-membered heterocyclic rings, are bonded to two carbon atoms and donate two p-electrons to the π-conjugated system. In the case of the Pt/NRGO sample, an additional component at 397.7 eV had to be included in the fit. To the best of our knowledge, no such a low BE component has been so far reported in literature for the N 1s peak in related systems. We suggest a correlation of such component with the effects of a strong Pt-N interaction. However, it is rather difficult to relate it to a specific type of N atom. It is interesting to highlight that this Pt-N component contributes significantly (25.1 %) to the whole N 1s peak area.

Table 2. Deconvolution of the C 1s XPS data into single chemical components for the carbon substrates and Pt/C catalysts. For each single chemical component, the BE (eV), FWHM (eV) and amount (%) values are given.

	C sp^2	C sp^3	C-N	Alcohols	Epoxy groups	Carbonyl groups	Carboxylic groups
Graphite	284.2 eV 0.52 86.5 %	285.3 eV 1.4 7.5 %	---	286.4 eV 1.4 5.1 %	---	287.9 eV 1.2 0.9 %	---
GO	284.1 eV 1.33 49.8 %	---	---	286.2 eV 1.03 38.8 %	287 eV 0.77 2.7 %	287.9 eV 1.37 7.0 %	288.9 eV 1.4 1.7 %
NRGO	284.4 eV 0.83 64.8 %	---	285.5 eV 1.3 17.1 %	286.4 eV 1.19 5.0 %	287.2 eV 1.03 4.2 %	288.0 eV 1.4 6.7 %	288.9 eV 1.4 2.2 %
Vulcan	284.4 eV 0.85 93.7 %	285.6 eV 1.2 4.1 %	---	286.3 eV 0.7 2.2 %	---	---	---
Pt/Graphite	284.2 eV 0.53 87.6 %	285.3 eV 1.3 4.1 %	---	286.3 eV 1.4 6.0 %	---	287.9 eV 1.4 2.3 %	---
Pt/RGO	284.2 eV 0.72 92.5 %	285.6 eV 0.8 3.8 %	---	286.3 eV 0.6 1.6 %	287 eV 1.4 2.1 %	---	---
Pt/NRGO	284.3 eV 0.88 67.5 %	---	285.4 eV 1.3 14.7 %	286.4 eV 1.06 5.0 %	287.2 eV 0.85 3.5 %	287.9 eV 1.25 6.4 %	288.9 eV 1.4 2.9 %
Pt/Vulcan	284.2 eV 0.89 89.9 %	285.4 eV 1.4 3.5 %	---	286.3 eV 1.0 6.6 %	---	---	---

Table 3. Deconvolution of the N 1s XPS data into single chemical components for the NRGO and Pt/NRGO materials. For each single chemical component, the BE (eV), FWHM (eV) and amount (%) values are given.

	Pt-N	Pyridinic	Pyrrolic	Graphitic	NO_x
NRGO	---	398.4 1.4 42.6 %	399.7 1.38 46.4 %	401.2 1.19 6.5 %	402.7 1.4 4.5 %
Pt/NRGO	397.7 1.0 25.1	398.7 1.4 35.2 %	399.8 1.36 28.6 %	401.2 1.07 5.0 %	402.5 1.4 6.1 %

	%				

Regarding the Pt 4f region, the spectra contain two peaks, which correspond to Pt $4f_{7/2}$ and $4f_{5/2}$ states from the spin-orbital splitting, and each peak was deconvoluted into three different Pt oxidation states (Pt^0, Pt^{2+} and Pt^{4+}) to identify the predominant oxidation state of Pt. As seen in Table 4, Pt^0 is the predominant oxidation state in all the Pt catalysts (around 54–66%) except in the Pt/NRGO, where the Pt^0 and Pt^{+2} species are comparable. The higher amount of Pt^{+2} species in the Pt/NRGO sample could also be interpreted as an evidence of the Pt-N interaction. This effect has been already reported in ref. [62]. On the other hand, all samples present a variable amount of Pt^{+2}

and Pt^{+4} species, deduced from the Pt $4f_{7/2}$ peaks at 72.1–74.6 eV. Their presence in all the samples can be attributed to the contact of the Pt NPs surface with air giving rise to Pt oxide phases. The fact that there is a considerable amount of oxidized species could be attributed to the small size of the Pt NPs (determined by TEM), resulting in a high percentage of Pt atoms on the surface of the NPs. A decrease in the amount of oxidized species can be observed for Pt/graphite and Pt/RGO samples. This can be associated with the formation of Pt islands resulting from the coalescence of small Pt nanoparticles leading to the formation of nanostructures possessing a higher crystallite size and consequently showing a different interaction with oxygen from the air. We note that the presence of oxides in supported Pd nanoparticles has been recently reported based on X-ray photoelectron spectroscopy analysis.[59] The presence of positively charged Pt ions could also suggest that there is an electron transfer from the Pt NPs to the underlying carbon support. The electron transfer from the Pt NPs to the carbon support has already been confirmed by theoretical calculations and experimental observations.[60-62] Moreover, there is a positive shift of around 0.3 eV of the Pt^0 component for the Pt/NRGO sample (71.2 eV), compared with the Pt/RGO sample (70.9 eV). This shift in the BE could confirm the electronic transfer from the Pt NPs to the carbon support through the N groups and be related to the Pt-N interactions observed in the N 1s photoemission at the lowest BE. In the literature, the Pt core-level f-band modification associated to N-doping effects has already been observed,[28, 62] and it has been stated that the N functional groups might increase the electron affinity of the substrate, facilitating the Pt electron donation behavior, which may be the main reason for the improved Pt catalytic activity and durability of the N-doped Pt/C systems compared to the undoped Pt/C ones. We come back to this point in our DFT analysis in a later section.

Table 4. Deconvolution of the Pt 4f XPS data into single chemical components for the Pt/C catalysts. For each single chemical component, the BE (eV), FWHM (eV) and amount (%) values are given.

	Pt^0	Pt^{2+}	Pt^{4+}
Pt/Graphite	71.0 0.9 65.7 %	72.2 1.4 26.5 %	74.6 1.6 7.8 %
Pt/Vulcan	71.2 1.0 54.5 %	72.4 1.4 31.5 %	74.1 1.5 14 %
Pt/RGO	70.9 0.9 66 %	72.2 1.5 21 %	73.9 1.6 13 %
Pt/NRGO	71.2 1.0 40.2 %	72.1 1.6 41.6 %	73.7 1.8 18.2 %

3.2 Electrochemical measurements

The electrocatalytic properties of the prepared graphene-supported Pt nanocatalysts were studied using cyclic voltammetry (CV) and rotating-disk electrode (RDE). Results are shown in **Figure 4**. **Figure 4a** shows CV curves of the investigated electrocatalysts in the potential range varying from 0.05 to 1.2 V/RHE. The CV curves showed two distinctive potential regions associated with hydrogen adsorption/ desorption process (H_{upd}) between 0.05 and 0.4 V/RHE, and with Pt oxidation beyond 0.7 V/RHE, where H_{upd} refers to the under-potential deposition of hydrogen. Platinum electrochemical surface area (ESA) values, calculated from H_{upd} region, assuming a charge transfer of 210 μC cm^{-2} on Pt surface,[63] were 34 m^2 g^{-1}, 28 m^2 g^{-1} and 20 m^2 g^{-1} for Pt/NRGO, Pt/RGO and Pt/Graphite catalysts, respectively, indicating that the utilization of Pt/NRGO and Pt/RGO were approaching that of conventional Pt/Vulcan catalyst with 30 m^2 g^{-1} (**see Table 5**). Additionally, in comparison with Pt/Vulcan, Pt/RGO, Pt/Graphite and Pt/NRGO showed higher potentials for the Pt oxide reduction peak, revealing that the Pt surface can be reduced at higher potentials, which can lead to an enhancement of the ORR activity. It should be noticed that the –OH formation at the surface of Pt/NRGO catalyst is to some extent inhibited in comparison with the other catalysts. The inhibition for H_2O activation is well-known to be responsible for enhancing the activity of Pt towards ORR.[64] This fact is greatly supported by XPS results with a down-shift BE of Pt 4f electrons. A similar effect was previously reported and contributes to the beneficial strong interaction between Pt-C hybridization.[5, 18]

The ORR polarization curves obtained with the investigated samples are shown in **Figure 4b**. It can be seen that Pt/NRGO shows a remarkably high electrocatalytic activity towards ORR in acid medium since the half-wave potential was *ca.* 0.825 V/RHE and largely higher than what can be obtained (*ca.* 0.795 V/RHE) with the conventional Pt/Vulcan catalyst, whereas half-wave potentials were respectively 0.820 V/RHE and 0.785 V/RHE for Pt/RGO and Pt/Graphite catalysts (**see Table 5**). Further kinetic information on the electron-transfer reaction mediated by the Pt/NRGO, Pt/RGO, Pt/Graphite catalysts in comparison with Pt/Vulcan catalyst, is shown in **Figure 4c**. It shows Tafel plots after mass-transfer correction. The Tafel slopes indicate that the reaction pathway and the rate-determining step are similar for Pt/RGO (81.4 mV dec^{-1}), Pt/Graphite (84.6 mV dec^{-1}) and Pt/Vulcan (85.2 mV dec^{-1}) catalysts, whereas a small variation of the Tafel slope can be observed with Pt/NRGO (95.3 mV dec^{-1}) materials (see **Table 5**). This can be associated with a different adsorption isotherm and with a different rate determining step. The kinetic current was calculated from the ORR curves according to the Koutecky-Levich equation[65] as follows:

$$\frac{1}{j} = \frac{1}{j_d} + \frac{1}{j_k} \quad (2)$$

where j is the measured current, j_d is the diffusion-limiting current, and j_k is the kinetic current. The kinetic current was calculated by the equation:

$$j_k = \frac{j \times j_d}{j_d - j} \quad (3)$$

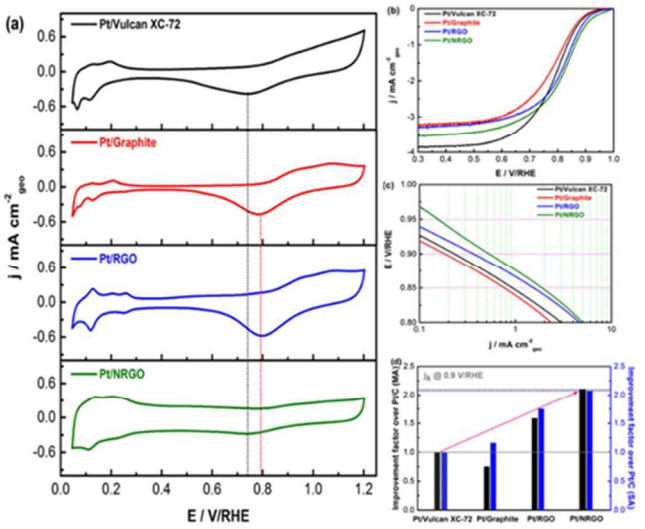

Figure 4. Comparison of catalytic properties of carbon supported Pt electrocatalysts. (a) CV curves recorded at 25 °C in N_2-saturated 0.5 M H_2SO_4 at a scan rate of 50 mV s^{-1}. (b) ORR curves in an O_2-saturated 0.5 M H_2SO_4 at a scan rate of 5 mV s^{-1} and a rotating rate of 900 rpm. (c) Tafel slopes extracted from ORR polarization curves. (d) Relative mass activity (MA, black color) and relative specific activity (SA, blue color) at 0.9 V vs. RHE for the investigated electrocatalysts. Mass and specific activities are given as kinetic current densities (j_k) normalized to the loading amount and electrochemical surface active area (ESA) of Pt, respectively.

Additionally, it is obvious that the kinetic current densities of Pt/NRGO and Pt/RGO are higher than that of Pt/Vulcan highlighting the improved ORR activities on graphene-supported Pt catalysts.

The mass and specific activities at 0.9 V/RHE for all the investigated catalysts are reported in **Figure 4d**. It can be observed that Pt/NRGO exhibits a mass activity, which is 2.1-fold higher than that of conventional Pt/Vulcan catalyst. Moreover, Pt/RGO displays a mass activity, which is 1.6-fold higher than that of Pt/Vulcan catalyst. In contrast, Pt/Graphite shows the lowest mass activity in reason of the low utilization of Pt in this sample. This is in agreement with the calculated ESA values.[66] Interestingly, the specific activities of Pt/NRGO, Pt/RGO and Pt/Graphite are higher than that obtained with conventional Pt/Vulcan catalyst. This difference in ORR activity most likely arises from the electronic modification of Pt generated by the substrate effect.

Table 5. Electrochemical active surface area (ESA), half-wave potential ($E_{1/2}$) and Tafel slopes calculated from the H_{upd} and ORR polarization curves of carbon supported Pt electrocatalysts.

	ESA (m^2 g^{-1})	$E_{1/2}$ (V *vs.* RHE)	Tafel slope (mV dec^{-1})
Pt/NRGO	34	0.825	95.3
Pt/ RGO	28	0.820	81.4
Pt/Graphite	20	0.785	84.6
Pt/Vulcan	30	0.795	85.2

3.3 Theoretical considerations

Properties of the support. The presence of the functional groups and dopants affect the geometric and electronic properties of the carbon support. The geometric changes are very small leading to a slight increase in the lattice parameters and bond distances. However, the changes in the electronic structure are more evident as the functional groups and nitrogen are more electronegative as shown by their Bader charges (Supporting Information **Table S1**). Therefore, the Density of States (DOS) of the studied systems present interesting features as depicted in **Figure 5**. The electronic population distribution of graphene is observed in **Figure 5a**. The addition of pyridinic N leads to the formation of new states especially at the Fermi level (**Figure 5a'**). These new states will be responsible for enhancement of the electric conductivity as they increase the metallic behavior of the system. Another peak at ~ -1.0 eV (below the Fermi level) may be responsible for a higher number of electrons available for transfer during the interactions of the surface with metallic clusters or molecules. The electronic structure of graphene oxide changes significantly as the amount of functional groups is raised (**Figures 5b, b', c,** and **c'**). When the quantity of oxygenated functional groups is higher (HOG) the system becomes semiconductor with a band gap close to ~3.0 eV (Figure 5c); for LOG conditions the system is still metallic but O and OH almost discrete states are present below and above the vicinity of the Fermi level (**Figure 5b**). The addition of a single N atom (~ 3% at.) causes changes in the DOS of GO, under LO conditions there is broadening of the distribution of states near the Fermi level but the influence is less dramatic since the system was already metallic (**Figure 5b'**), but for HOG the band gap decreases by ~0.5 eV (**Figure 5c'**).

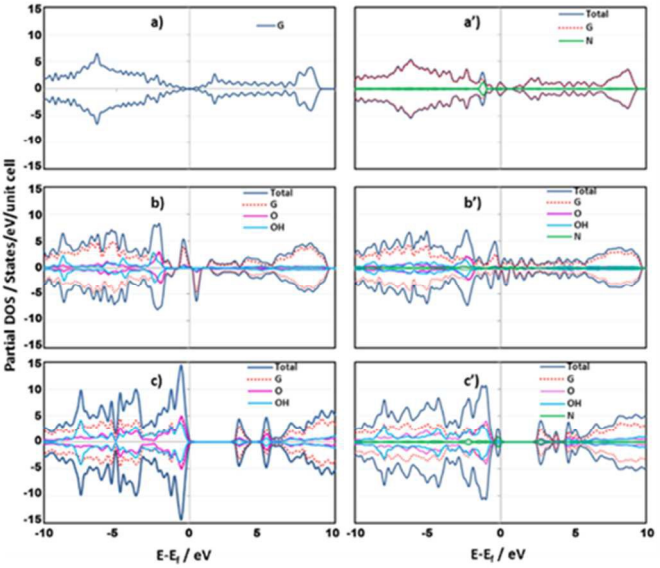

Figure 5. Partial DOS (in states/eV) for the studied support materials: a) Graphene, a') N-doped graphene, b) LOG, b') N-doped LOG, c) HOG and c') N-doped HOG. Positive and negative DOS branches represent spin up and down electrons respectively. The horizontal axis displays relative energies E-E_f (in eV) where E_f is the Fermi level.

Interaction of the substrate with Pt_4. A Pt_4 cluster was relaxed in the tetrahedral geometry, and once optimized it was allowed to interact with the support. **Figure S2** depicts the Pt_4 cluster interacting with O_2, and supported clusters interacting with nitrogen doped supports. **Figure S3** depicts the interaction of the cluster with LOG and HOG. The interaction energy (E_{int}) of the cluster with the

support was calculated as the energy difference between the separated systems and the resultant geometry after the relaxation procedure. **Table 6** indicates that E_{int} varies depending on the structure of the support and the participating site. Several structures and sites were analyzed; however, as the size of the cluster is very small and has a low cohesive energy, in some cases the deformation of the cluster is very large. It should be noted that the interaction energy calculated in this way does not take into account cluster deformation which is observed as a consequence of this interaction. Nevertheless, the interaction of the support with this small cluster is strong and all effects resultant from this interaction are enhanced with respect to the unsupported cluster. For example, reactivity trends of CO adsorption on supported clusters are qualitatively well represented,[67, 68] while quantitative information can be obtained analyzing the interaction of the support with a larger cluster, as reported in a later section.

The weakest metal-substrate interaction is obtained with the intrinsic sites of the graphene layer (Table 6); stronger effects depend on the specific site and closeness of the metallic sites from the functional groups that decorate the support. In the case of the structures doped with nitrogen (G-1N and G3-N) the interaction energy is more than twice that obtained with graphene (Table 6). Stronger metal/support interaction energies represent advantages in fuel cell electrocatalysts where the mobility and aggregation of the cluster is one of the main problems associated to durability. The stronger metal-support interactions for N-doped graphene are in agreement with the TEM images of the N-doped support revealing well distributed particles while all other samples show evidence of particle agglomeration. The interaction of the cluster with three nitrogen atoms-support (G-3N) not only enhances the interaction energy but leads to a higher charge transfer from the cluster to the support as shown by the average Pt charge in Table 6, in agreement with the observations reported by Gracia Espino et al.[69] in core-shell Pt-Ni clusters. The extent of charge transfer is a very important property for the catalytic activity because electron transfer from the metal directed towards the support may limit the metallic surface ability to provide electrons for the chemical or electrochemical reduction reactions. Stronger metal/support interaction energy is found for GO in all of the oxidation states and in presence of functional groups. The degree of oxidation also affects the interactions: in LOG the smaller amount of functional groups allows the cluster atoms to interact mostly with carbon atoms; whereas in the HOG the cluster is able to mostly interact with the functional groups instead of carbon. Therefore, in the OH side of LOG, when the cluster is interacting totally with carbon atoms the interaction energy is stronger than in graphene but the charge transfer is similar to that in graphene. Conversely, in the O side of HOG the cluster is totally in contact with the epoxy groups and not interacting with carbon atoms. At these conditions, the interaction energy is weaker but the charge transfer is very high. The most significant charge transfer is obtained in the O side of the LOG, where the cluster interacts with carbon atoms in the support but also with oxygen atoms of the epoxy groups. Therefore, in general the oxygen functional groups enhance the metal-substrate interaction strength and lead to higher charge transfer but an excessive amount of oxygenated groups as in HOG offers disadvantages. This is primarily because of the HOG semiconducting behavior discussed above and secondly because of the higher feasibility of oxidation and formation of CO_2. The addition of nitrogen to GO slightly modifies the interaction energy strength and enhances the charge transfer but only when the cluster interacts directly with the nitrogen atom, in any other case the behavior is very similar to the non-nitrogenated substrates.

Under the effect of O_2 adsorption the deformation of the cluster was found to be more severe, thus only the simulations in which the cluster retains its original shape are reported. The adsorption was modeled by addition of O_2 directly on one of the bridge sites of the cluster. It is worth mentioning that in the unsupported cluster the adsorption of oxygen is the strongest compared to those on any of the supported clusters. The distance Pt-O_2 also changes. Two Pt-O distances are reported in Table 6 (last column): the first corresponds to the oxygen adsorbed on a Pt atom not interacting with the support while the second corresponds to the Pt atom interacting directly with the support. On the unsupported Pt cluster both of them are equal, but in the supported clusters the first is shorter and the second larger, indicating that the interaction of Pt with the support causes weaker oxygen adsorption (larger Pt-O distance) especially near the Pt-support interface. The charge transferred from the cluster to the adsorbate is higher when the cluster is only donating electrons to the O_2 molecule. The presence of the C support diminishes the O_2 adsorption energy (Table 6 and Figure S2) and also reduces the amount of charge that is transferred from the cluster to O_2 because the cluster is also donating charge to the support. Therefore the distances O-Pt are larger and the O-O distance is shorter (Table 6 and Figures S2-a, and -b) i.e. the reduction of O_2 is more difficult.

The interaction of Pt_4 with N-doped graphene causes stronger O_2 adsorption than that in Pt_4-graphene but still weaker than that on the unsupported cluster. The Pt-O distances are shorter than those in Pt_4-graphene and the unsupported case. Also the charge transfer to the adsorbate (Table 6) is even higher than that in the unsupported case. Moreover, a higher number of dopant N atoms (G-3N) enhances this charge transfer to O_2 leading to an elongated O-O distance indicating that the mere presence of nitrogen is able to facilitate the O-O bond breaking, again in agreement with the analysis of Gracia Espino et al..[69] For the interaction with GO, the charge transferred from Pt_4 to O_2 is lower indicating that the presence of oxygenated species in the support (because of the oxygen higher electronegativity) causes electron retention. Part of these electrons are needed for the cluster-substrate interaction; therefore, especially in the O-side of the HOG in which the cluster interacts totally with oxygen atoms and not with carbon atoms the charge transfer is the lowest and the O-O distance becomes only slightly higher than its gas phase value while the Pt-O distances are large. Especial attention deserves the LOG in the O-side (**Figure S3b**) which presents higher charge transfer to O_2 and the largest O-O distance; in this case the Pt_4 cluster interacts with epoxy groups but with carbon atoms as well. This scenario seems to be favorable for O_2 reduction suggesting that a lower amount of decorating functional groups is more favorable for reactivity. Note that the geometry of the cluster also changes significantly in this case.

The analysis of the interaction of a small cluster with doped and functionalized supports led us to conclude that charge transfer from the support to the adsorbed molecule is a very important property. If the dopant or functional groups retain the electrons very strongly, the cluster will have a limited capacity to donate electrons to O_2 but if the cluster can receive electrons from the support and is able to donate them during the catalytic reaction then the catalytic activity could be enhanced.

The experimental results of N-doped graphene reported nitrogen concentrations close to 15% at. In the simulations reported so far, the N concentration was close to 3% at. N. The simulations in this section are aimed to better represent the effect of the N-doped support on a more realistic nanoparticle size and higher N concentrations. A Pt_{38} cluster ~0.8 nm diameter was allowed to interact with a 7x7 graphene layer. To model the interaction with N-doped graphene support two degrees of doping were used: 3N-doped (N 3% at) and 6N-doped (N 6 % at). The 3N-doped was simulated by eliminating one carbon atom and exchanging the carbon atoms with dangling bonds by N. For the 6N-doped three carbon atoms

were eliminated and the formed carbon dangling bonds were exchanged with pyridinic nitrogen. The influence of oxygenated functional groups is supposed to be minimal according to the experimentally found low concentration of oxygenated species. For the cluster Pt_{38} interacting with the 3N-doped graphene, the three nitrogen atoms interact only with one Pt atom while the other Pt atoms are interacting with carbon atoms (Figure S4-c); on the other hand on the 6N-doped support each nitrogen interacts with a platinum atom at the interface, so six out of seven Pt atoms at the interface are interacting with nitrogen (Figure S4-d). It is important to point out that the DFT results suggest the formation of Pt-N bonds observed both in the Pt_4 and Pt_{38} models (Figures S2-c and –d, and S4-c and -d respectively), in agreement with the conclusions from our XPS experiments and also with previous calculations.[69]

Table 6. DFT calculated interaction of Pt_4 with the various supports and changes in O_2 adsorption energy.

		S-Pt_4			S-Pt_4-O_2			
		E_{int} / eV	Pt-C / Å	Pt Charge / a.u.	Oxygen Ads / eV	O-O distance	O_2 charge	O-Pt
Pt_4				0.0	-1.97	1.438	-0.61	1.971 - 1.974
Graphene		-1.15	2.28 (Bridge)	+0.10	-1.33	1.396	-0.57	1.989 - 2.037
G-1N		-2.74	2.04 (2.15 – N)	+0.26	-1.41	1.430	-0.64	1.898 - 1.948
G-3N		-2.43	(2.13 – N)	+0.44	-1.50	1.451	-0.65	1.891 - 1.931
LOG	OH side	-2.67	2.18	+0.16	-1.33	1.386	-0.57	1.960 - 2.095
	O side	-7.85	2.23 (2.01 – O)	+0.98	-1.26	1.493	-0.63	1.902 - 1.923
HOG	OH side	-1.89	2.25 (2.01 – O)	+0.55				
	O side	-2.01	(2.14 – O)	+0.78	-1.35	1.398	-0.56	2.028 - 1.988
LOG-N		-2.8	2.12 (2.10 – N)	+0.34				
HOG-N		-2.16		+0.89				

Properties of the support. Figure 6 shows the density of states of the graphene sheet compared with those of the doped graphene with various N concentrations. As discussed above, new states arise near the Fermi level and those are enhanced with a higher N concentration. There is also a higher charge transfer from carbon atoms to nitrogen being reflected on the total charge of the graphitic structure. **Table S2** reports the total charge donated as the amount of nitrogen increases. The interaction energy was calculated as in the

previous section. However, here we included the deformation effects of both support and cluster. **Table S2** shows that for graphene the interaction energy is very weak even becoming slightly positive if the deformation is not taken into account, also charge transfer occurs, but graphene donates a small amount of charge to the cluster. For N-doped graphene the interaction energy without considering deformation effects is stronger compared to pure graphene and is enhanced as the N concentration increases. However if the deformation is taken into account the interaction energies of the cluster with the two N-doped substrates are comparable but very strong in comparison to that of the cluster supported on graphene, thus confirming the strong cluster/support interaction in the N-doped substrate.

Also the charge transfer follows the same trend observed in Pt_4 in which the Pt cluster donates charge to N and carbon atoms. In Supporting Information **Figure S4**, the geometry of the Pt_{38} cluster is depicted showing the main (111) and (100) planes. The clusters interact with the support through one of the (111) planes, and as the number of N atoms increases the cluster becomes closer to the support due to strong Pt-N interactions. We acknowledge that for this cluster size, other morphologies may also be present in fuel cell environments. Previous DFT studies of growth of Pt clusters[70] have determined that clusters evolve from icosahedral type (approximately 13-38 atoms) towards fcc-like (> 38 atoms). Thus we may expect a mixture of icosahedral and fcc-like clusters at this cluster size.

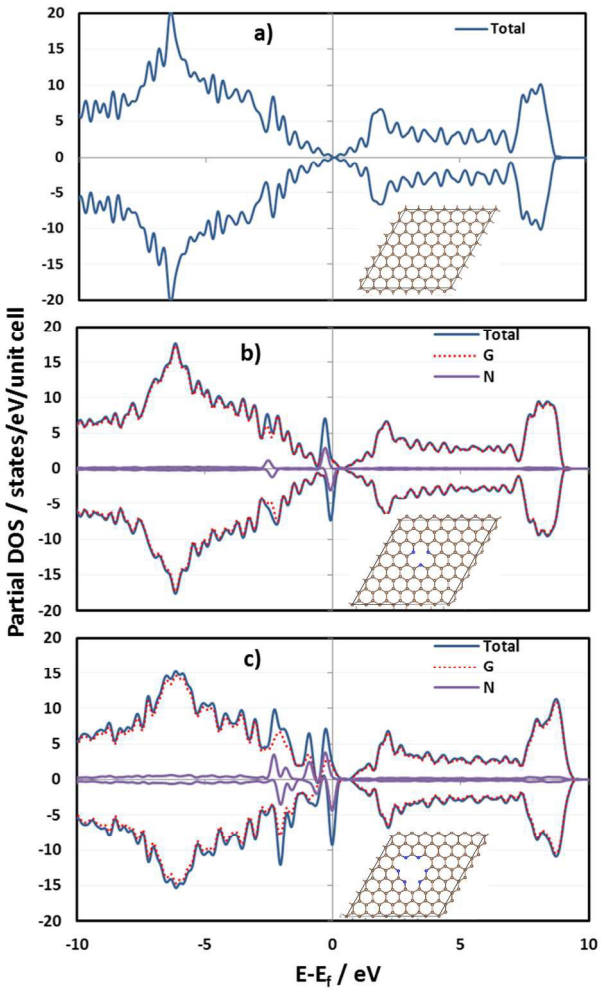

Figure 6. Partial DOS (in states/eV) of the support a) graphene, b) 3N-doped graphene and c) 6N-doped graphene. Insets show the structure, carbon atoms in brown and nitrogen in blue spheres.

Electronic properties of the supported Pt_{38} cluster. The partial DOS of the cluster is depicted in **Figure 7**. To identify contributions from interfacial atoms and atoms in the top of the cluster they are shown separately. In the unsupported case there are no interfacial atoms; therefore both sides of the cluster, as the cluster is symmetrical, are the same. For the supported cluster, the partial DOS of interfacial atoms are very different to those of the atoms located at the top of the cluster (far from the support). Moreover, the DOS at the top of the cluster are shifted slightly towards more positive values than the unsupported cluster. For the atoms in the upper part of the cluster a relatively large shift toward the Fermi level is found with respect to the DOS of the unsupported cluster when the cluster interacts with graphene, and with G-3N and G-6N. On the other hand, the interaction of G-6N with the cluster atoms at the interface with the substrate leads to higher changes. These changes are expected to have an effect on the catalytic behavior of the nanoparticles, O_2 and O adsorption (key stages in the oxygen reduction) as discussed in the next section.

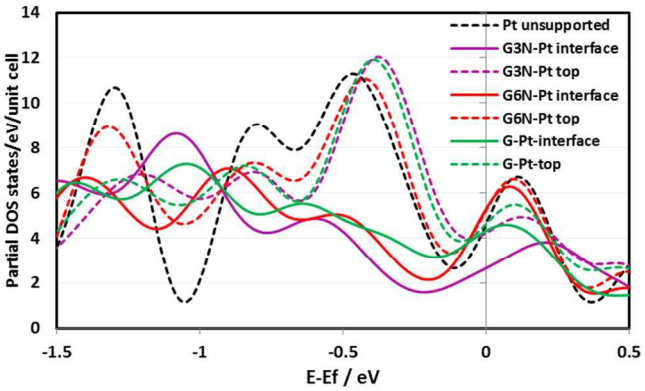

Figure 7. Partial density of states (in states/eV) vs. relative energies E-E_f where E_f is the energy of the Fermi level. Contributions of Pt atoms at the top of the cluster and at the interface are separated for the supported cluster. The DOS for the unsupported cluster (involving all atoms) is also shown.

Table 7 reports the calculated O_2 and O adsorption energies on top of the cluster. The O_2 adsorption energies in the various systems are very comparable. However, they are weaker compared to the case of the unsupported cluster. . On the other hand, the O-O distance is shorter in the unsupported cluster while the effect of the support facilitates O_2 dissociation leading to slightly longer O-O distances. Although these differences are small, and the changes in charge transfer to the adsorbate are also small, the supported cases always lead to higher charge transfer in comparison to graphene.

Journal Name RSCPublishing

ARTICLE

Table 7. Adsorption energies and properties of O_2 and O on Pt_{38} unsupported and over the supports discussed in this study.

	Pt_{38}-O_2							Pt_{38}-O				
	E_{ads} (eV)	d / Å		Charges (e)				E_{ads} (eV)	Charges (e)			
		O-O	Pt-O	G	N	Pt	O_2		G	N	Pt	O
Pt_{38}	-1.42	1.401	1.953	-	-	0.5764	-0.5764	-4.98	-	-	0.6760	-0.6760
G-Pt_{38}	-1.39	1.410	1.956	0.1318	-	0.4993	-0.6310	-4.79	0.1032	-	0.5836	-0.6865
G3N-Pt_{38}	-1.38	1.411	1.948	2.8106	-3.0126	0.8221	-0.6199	-4.83	2.7955	-3.033	0.9275	-0.6900
G6N-Pt_{38}	-1.31	1.410	1.953	5.9439	-6.3993	1.0685	-0.6128	-4.81	5.9056	-6.3406	1.1208	-0.6859

The presence of nitrogen makes the extent of the charge donation from the cluster to the adsorbed molecule slightly lower in comparison to the trends observed for the small Pt_4 cluster.

We also evaluated the adsorption of atomic oxygen, to have a measure of the interactions with the ORR intermediate species. The strongest O adsorption is found on the unsupported cluster, whereas it is slightly weaker on all supported clusters; however the differences between doped and non-doped are small and no significant differences are observed as the concentration of dopant is increased. On the other hand, the charge transfer from the cluster to the adsorbed molecule is higher on supported clusters; however, the extent of charge donation seems to be smaller as the N concentration in the support increases. Finding materials that adsorb oxygenated compounds slightly weaker than on Pt may represent advantages for the oxygen reduction reaction. This is especially important for the OH species which can poison the catalyst if strongly adsorbed. Therefore the interaction of the supported metallic cluster may be beneficial because of the weaker adsorption of oxygenated species. In addition, as the interaction of the cluster with the support is higher in the doped support, this will provide enhanced stability.

Finally, given that the influence of the support can be greater or lower depending on the location of the O_2 adsorption site on the nanoparticle surface. To probe this statement we allowed O_2adsorption in two additional sites, one at the middle of the cluster and another in a site in which one of the oxygen atoms is interacting directly with a Pt atom located at the interface (Supporting Information, **Figure S5** depicts the sites for O adsorption in the three cases). The position of oxygen is similar in the supported clusters i.e. in the same type of cluster facet (111), bridge site in atoms with similar connectivity; the only difference is in the closeness respect to the support). We note that the spin polarization distribution in both Pt_4 and Pt_{38} may be also affected by the adsorption of the oxygenated species probably also affecting their reactivity.

The values for O_2 adsorption reported in **Table 8** indicate that the effect of the support is accentuated when the molecules are closer to the support. Two values for adsorption energy are reported, one calculated without considering the changes in geometry after adsorption and the second including the geometry changes. Results for adsorption on the top of the cluster without cluster reconstruction the results have already been discussed in the previous section. For O_2 locations at the middle of the cluster surface the adsorption in all cases is weaker (than in the unsupported case and that in the top of the cluster); among them the G-3N is considerably weaker than all the others. At the cluster-support interface the G-3N support leads to the lowest adsorption energy. In the G and G-6N supports, even though the initial site and geometry for oxygen adsorption in the three supports was the same, the oxygen molecule tends to migrate from the interface to the middle leading to adsorption in a hollow site (**Figure 8**). After migration the adsorption is stronger (even stronger than in the supported case for Pt_{38}-G and very similar to the unsupported case in Pt_{38}-G-6N). In order to compare the O_2 adsorption in the same site, a new simulation in a hollow site in the G-3N was performed (value in parenthesis in **Table 8**). In that case the O-O distance is longer and the charge transferred to the O_2 molecule is larger, confirming an additional higher effect owed to the N-doped support. When the reconstruction is taken into account the same trends are observed. However the O_2 adsorption on top of the G-Pt_{38} is stronger than that in the unsupported case, while for O_2 adsorptions closer to the support the presence of N-species in the support leads to a weaker O_2 adsorption.

To investigate this point, it is useful to examine the interactions between the cluster and the support. In some cases the adsorption of O_2 has an effect on the separation between the cluster and the support. When adsorption is allowed in the top or in the middle of the cluster the changes in cluster/support separation for all the supports are negligible; however, when O_2 is very close to the interface the distance cluster-support is

elongated, especially in the undoped graphene-supported cluster where the changes lead to the an almost total separation of the cluster from the support. In contrast, in the G-3N case only two of the interacting platinum atoms are slightly more separated from the support and

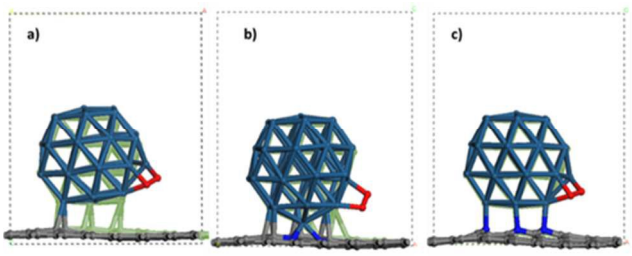

Figure 8. Final configuration of the adsorption of oxygen at the cluster-support interface (Pt, C and O in blue, gray and red spheres respectively). The initial geometry of the supported cluster without oxygen is depicted in the back as green shadows. a) Pt_{38}-G, b) Pt_{38}-G-3N and c) Pt_{38}-G-6N.

in the G-6N support the connectivity of the cluster remained the same (**Figure 8**). Therefore, this confirms that the strong interaction with the nitrogen-doped support besides enhancing the catalytic activity may also lead to a higher stability. Moreover, the differences in catalytic activity of Pt on the N-doped support can also be related to a stronger metal-substrate interaction which leads to no changes in the cluster-support separation in the presence of oxygen. On the contrary, the separation between the cluster and support in the non-doped system could lead to a higher resistance for electron transfer. Interestingly, the interaction of the cluster with only pyridinic nitrogen does not lead to a further enhancement of the catalytic activity; the presence of carbon and nitrogen atoms interacting with the cluster is the best option to enhance both the catalytic activity and stability of the nanoparticle for cathodes in fuel cells, cf. section 3.2.

Table 8. O_2 adsorption energy (in eV) in Pt_{38} as a function of the adsorption site. The first value is the total adsorption energy and the second value (after the slash) is the adsorption energy taking into account the deformation of both cluster and support. Value in parenthesis for adsorption at the interface in the Pt_{38}-G-3N corresponds to the hollow site.

	Top	Middle			Interface		
Pt_{38}-unsupported	-1.42/-1.96	E_{ads}	O-O / Å	B.C / e^-	E_{ads}	O-O / Å	B.C / e^-
Pt_{38}-G	-1.39/-2.01	1.37/-1.97	1.4093	-0.62	-1.90/-2.18	1.4827	-0.73
Pt_{38}-G-3N	-1.38/-1.96	1.19/-1.63	1.4092	-0.61	-0.97/-1.27 (-1.71/-2.18)	1.3813 (1.4896)	-0.55 (-0.75)
Pt_{38}-G-6N	-1.31/-1.82	-1.33/-1.87	1.4051	-0.61	-1.43/-2.03	1.4837	-0.74

4. Conclusions

In this study, low-mass loading catalysts (*ca.* 5 wt. % Pt/C) were synthesized via the carbonyl chemical route allowing for the heterogeneous deposition of Pt nanoparticles onto different carbon-based substrates. N-doped RGO, RGO, GO graphite and Vulcan XC-72 were used as substrates. Raman spectroscopy showed that except for graphite all the graphitic materials investigated in this study presented low inter-defect lengths. On the N-doped material, the XPS data analysis revealed that the N 1s photoemission line can be deconvoluted into different chemical signatures namely, pyridinic, pyrrolic, graphitic and oxidized nitrogen. The main components were pyridinic and pyrrolic species. The examination of Pt 4f photoemission peaks showed that a non-negligible amount of Pt atoms (25%) are chemically bound to N atoms, which was confirmed by the DFT analysis. This strong interaction between Pt clusters and N atoms allows for an electronic transfer from Pt to the carbon support, also predicted by our DFT calculations. Electrochemical measurements have shown that NRGO as substrates led to an increase in the mass activity of the catalyst at 0.9 V vs. RHE. This can be related to changes in the oxygen adsorption energy at the platinum surface. DFT calculations show that the molecular and atomic oxygen adsorption is weaker for the N-containing substrates. The DFT results reveal that the O-O distance is much elongated in the case of the N-doped substrates, which suggests lower barriers for O_2 dissociation. This is a first point to explain the increased electrocatalytic activity of Pt/NRGO toward the ORR. It should be added that the weaker O_2 and O adsorption suggest that other oxygenated compounds, such as OH may also be weaker on the catalysts supported in the N-doped substrates, which would further enhance the catalytic activity given that strongly adsorbed OH is a well-known catalyst poison. Additionally, in contrast to the non-doped systems, calculations have shown that the strong interaction between Pt clusters and N-doped graphene led to no changes in cluster/support separation with the presence of adsorbed molecular oxygen. We suggest that this stronger interaction may be responsible for a decrease in the resistance for electron transfer between the cluster and the substrate facilitating the electrochemical reactions. All results obtained in this study are of major importance and lay the basis for the development and demonstration of new cathode architectures for low temperature proton exchange membrane fuel cells.

Acknowledgements

JM thanks the fellowship of "Ministère de l'Enseignement Supérieur et de la Recherche". GRS thanks CONACYT (Mexico) for the postdoctoral fellowship. The authors thank Mrs. C. Canaff for her technical assistance with XPS measurements. This work was partially supported by the European Union's Seventh Framework Programme (FP7/2007-2013) for the Fuel Cell and Hydrogen Joint Technology Initiative under grant agreement nr. 303492 CathCat.

Notes and references

[a] IC2MP, UMR-CNRS 7285, University of Poitiers, 4 rue Michel Brunet, 86022 Poitiers, France.
[b] Department of Chemical Engineering, Texas A&M University, College Station, TX 77843, United States.
[c] Department of Chemical Sciences, University of Padova, Via Marzolo 1, 35131 Padova, Italy.
[d] Faculty of Materials Science and Engineering, Hubei University, 430062 Wuhan, China.

* Corresponding Author: nicolas.alonso.vante@univ-poitiers.fr (NAV)

† Present Addresses
J. Ma: Sorbonne Universités, UPMC Université Paris 06, UMR-CNRS 8234, PHENIX, F-75005, Paris, France
G. Ramos-Sánchez: Cátedras Conacyt: Departamento de Química Universidad Autónoma Metropolitana – Iztapalapa.

Electronic Supplementary Information (ESI) available: [Views of 4×4, LOG and HOG graphene sheets considered for calculations, views of interaction of oxygen with Pt_4 clusters supported on different substrates, views of Pt_{38} clusters interacting with different substrates, views of positions of O_2 interacting with Pt_{38} clusters supported on N3-doped graphene]. See DOI: 10.1039/b000000x/

1. M. K. Debe, *Nature*, 2012, **486**, 43-51.
2. H. A. Gasteiger, S. S. Kocha, B. Sompalli and F. T. Wagner, *Appl. Catal. B*, 2005, **56**, 9-35.
3. J. Wu and H. Yang, *Acc. Chem. Res.*, 2013, **46**, 1848-1857.
4. A. Manzo-Robledo, A. C. Boucher, E. Pastor and N. Alonso-Vante, *Fuel Cells*, 2002, **2**, 109-116.
5. J. Ma, A. Habrioux and N. Alonso-Vante, *ChemElectroChem*, 2014, **1**, 37-46.
6. F. Hasche, M. Oezaslan and P. Strasser, *Phys. Chem. Chem. Phys.*, 2010, **12**, 15251-15258.
7. Y.-C. Park, K. Kakinuma, M. Uchida, D. A. Tryk, T. Kamino, H. Uchida and M. Watanabe, *Electrochim. Acta*, 2013, **91**, 195-207.
8. A. Lewera, L. Timperman, A. Roguska and N. Alonso-Vante, *J. Phys. Chem. C*, 2011, **115**, 20153-20159.
9. L. Timperman, A. Lewera, W. Vogel and N. Alonso-Vante, *Electrochem. Commun.*, 2010, **12**, 1772-1775.
10. J. Ma, A. Habrioux and N. Alonso-Vante, *J. Solid State Electrochem.*, 2013, **17**, 1913-1921.
11. V. T. T. Ho, C.-J. Pan, J. Rick, W.-N. Su and B.-J. Hwang, *J. Am. Chem. Soc.*, 2011, **133**, 11716-11724.
12. C. V. Subban, Q. Zhou, A. Hu, T. E. Moylan, F. T. Wagner and F. J. DiSalvo, *J. Am. Chem. Soc.*, 2010, **132**, 17531-17536.
13. K. Gong, F. Du, Z. Xia, M. Durstock and L. Dai, *Science*, 2009, **323**, 760-764.
14. E. Yoo, T. Okata, T. Akita, M. Kohyama, J. Nakamura and I. Honma, *Nano Lett.*, 2009, **9**, 2255-2259.
15. C. Huang, C. Li and G. Shi, *Energy Environ. Sci.*, 2012, **5**, 8848-8868.
16. M. Liu, R. Zhang and W. Chen, *Chem. Rev.*, 2014, **114**, 5117-5160.
17. R. Siburian, T. Kondo and J. Nakamura, *J. Phys. Chem. C*, 2013, **117**, 3635-3645.
18. J. Ma, A. Habrioux, C. Morais, A. Lewera, W. Vogel, Y. Verde-Gómez, G. Ramos-Sanchez, P. B. Balbuena and N. Alonso-Vante, *ACS Catal.*, 2013, **3**, 1940-1950.
19. P. Xu, L. Dong, M. Neek-Amal, M. L. Ackerman, J. Yu, S. D. Barber, J. K. Schoelz, D. Qi, F. Xu, P. M. Thibado and F. M. Peeters, *ACS Nano*, 2014, **8**, 2697-2703.
20. D. He, K. Cheng, H. Li, T. Peng, F. Xu, S. Mu and M. Pan, *Langmuir*, 2012, **28**, 3979-3986.
21. D. He, Y. Jiang, H. Lv, M. Pan and S. Mu, *Appl. Catal. B*, 2013, **132–133**, 379-388.
22. G. He, Y. Song, K. Liu, A. Walter, S. Chen and S. Chen, *ACS Catal.*, 2013, **3**, 831-838.
23. J. Ma, A. Habrioux, N. Guignard and N. Alonso-Vante, *J. Phys. Chem. C*, 2012, **116**, 21788-21794.
24. H. Wang, T. Maiyalagan and X. Wang, *ACS Catal.*, 2012, **2**, 781-794.
25. J. Bai, Q. Zhu, Z. Lv, H. Dong, J. Yu and L. Dong, *Int. J. Hydrogen Energy*, 2013, **38**, 1413-1418.
26. A. Zahoor, M. Christy, Y. J. Hwang, Y. R. Lim, P. Kim and K. S. Nahm, *Appl. Catal. B*, 2014, **147**, 633-641.
27. H. Wang, M. Xie, L. Thia, A. Fisher and X. Wang, *J. Phys. Chem. C*, 2013, **5**, 119-125.
28. Y. Zhou, R. Pasquarelli, T. Holme, J. Berry, D. Ginley and R. O'Hayre, *J. Mater. Chem.*, 2009, **19**, 7830-7838.
29. W. S. Hummers and R. E. Offeman, *J. Am. Chem. Soc.*, 1958, **80**, 1339-1339.
30. N. Alonso-Vante, *Fuel Cells*, 2006, **6**, 182-189.
31. M. Wojdyr, *J. Appl. Crystallogr.*, 2010, **43**, 1126-1128.
32. S. Doniach and M. Sunjic, *Journal of Physics C: Solid State Physics*, 1970, **3**, 285.
33. R. J. W. E. Lahaye, H. K. Jeong, C. Y. Park and Y. H. Lee, *Phys. Rev. B*, 2009, **79**.
34. P. E. Blochl, *Phys. Rev. B*, 1994, **50**, 17953-17979.
35. G. Kresse and D. Joubert, *Phys. Rev. B*, 1999, **59**, 1758-1775.
36. G. Kresse and J. Furthmuller, *Comput. Mater. Sci.*, 1996, **6**, 15-50.
37. G. Kresse and J. Hafner, *Phys. Rev. B: Condens. Matter Mater. Phys.*, 1993, **48**, 13115-13118.
38. H. J. Monkhorst and J. D. Pack, *Phys. Rev. B*, 1976, **13**, 5188-5192.
39. J. Schwan, S. Ulrich, V. Batori, H. Ehrhardt and S. R. P. Silva, *J. Appl. Phys.*, 1996, **80**, 440-447.
40. J. Kohanoff, *Computational Materials Science*, 1994, **2**, 221-232.
41. R. E. Shroder, R. J. Nemanich and J. T. Glass, *Phys. Rev. B*, 1990, **41**, 3738-3745.
42. M. Veres, S. Tóth and M. Koós, *Diamond Relat. Mater.*, 2008, **17**, 1692-1696.
43. M. A. Pimenta, G. Dresselhaus, M. S. Dresselhaus, L. G. Cancado, A. Jorio and R. Saito, *Phys. Chem. Chem. Phys.*, 2007, **9**, 1276-1290.
44. L. C. Nistor, J. Landuyt, V. G. Ralchenko, T. V. Kononenko, E. D. Obraztsova and V. E. Strelnitsky, *Appl. Phys. A: Mater. Sci. Process.*, 1994, **58**, 137-144.
45. T. Jawhari, A. Roid and J. Casado, *Carbon*, 1995, **33**, 1561-1565.
46. E. F. Antunes, A. O. Lobo, E. J. Corat, V. J. Trava-Airoldi, A. A. Martin and C. Veríssimo, *Carbon*, 2006, **44**, 2202-2211.
47. V. Mennella, G. Monaco, L. Colangeli and E. Bussoletti, *Carbon*, 1995, **33**, 115-121.
48. X. M. Tang, J. Weber, S. N. Mikhailov, C. Müller, W. Hänni and H. E. Hintermann, *J. Non-Cryst. Solids*, 1995, **185**, 145-150.
49. A. Cuesta, P. Dhamelincourt, J. Laureyns, A. Martínez-Alonso and J. M. D. Tascón, *Carbon*, 1994, **32**, 1523-1532.
50. R. Vidano and D. B. Fischbach, *J. Am. Ceram. Soc.*, 1978, **61**, 13-17.
51. L. G. Cancado, K. Takai, T. Enoki, M. Endo, Y. A. Kim, H. Mizusaki, A. Jorio, L. N. Coelho, R. Magalhaes-Paniago and M. A. Pimenta, *Appl. Phys. Lett.*, 2006, **88**, 163106.
52. C. Galeano, J. C. Meier, V. Peinecke, H. Bongard, I. Katsounaros, A. A. Topalov, A. Lu, K. J. J. Mayrhofer and F. Schüth, *J. Am. Chem. Soc.*, 2012, **134**, 20457-20465.
53. C. Mattevi, G. Eda, S. Agnoli, S. Miller, K. A. Mkhoyan, O. Celik, D. Mastrogiovanni, G. Granozzi, E. Garfunkel and M. Chhowalla, *Adv. Funct. Mater.*, 2009, **19**, 2577-2583.
54. M. Favaro, S. Agnoli, C. Di Valentin, C. Mattevi, M. Cattelan, L. Artiglia, E. Magnano, F. Bondino, S. Nappini and G. Granozzi, *Carbon*, 2014, **68**, 319-329.
55. M. Favaro, L. Perini, S. Agnoli, C. Durante, G. Granozzi and A. Gennaro, *Electrochim. Acta*, 2013, **88**, 477-487.
56. M. Favaro, S. Agnoli, L. Perini, C. Durante, A. Gennaro and G. Granozzi, *Phys. Chem. Chem. Phys.*, 2013, **15**, 2923-2931.
57. W. Ju, M. Favaro, C. Durante, L. Perini, S. Agnoli, O. Schneider, U. Stimming and G. Granozzi, *Electrochim. Acta*, 2014, **141**, 89-101.
58. T. Sharifi , G. Hu , X. Jia , and T. Wågberg, *ACS Nano*, 2012, **6**, 8904-8912.
59. E. Gracia-Espino, G. Hu, A. Shchukarev and T. Wågberg, *J. Am. Chem. Soc.*, 2014, **136**, 6626-6633.
60. D.-H. Lim and J. Wilcox, *J. Phys. Chem. C*, 2011, **115**, 22742-22747.

61. T. Holme, Y. Zhou, R. Pasquarelli and R. O'Hayre, *Phys. Chem. Chem. Phys.*, 2010, **12**, 9461-9468.
62. Y. Zhou, T. Holme, J. Berry, T. R. Ohno, D. Ginley and R. O'Hayre, *J. Phys. Chem. C*, 2009, **114**, 506-515.
63. T. J. Schmidt, H. A. Gasteiger, G. D. Stäb, P. M. Urban, D. M. Kolb and R. J. Behm, *J. Electrochem. Soc.*, 1998, **145**, 2354-2358.
64. Y. Bing, H. Liu, L. Zhang, D. Ghosh and J. Zhang, *Chem. Soc. Rev.*, 2010, **39**, 2184-2202.
65. A. J. Bard and L. R. Faulkner, *Electrochemical methods. Fundamentals and applications*, Wiley, New York, 2001.
66. M. Uchida, Y.-C. Park, K. Kakinuma, H. Yano, D. A. Tryk, T. Kamino, H. Uchida and M. Watanabe, *Phys. Chem. Chem. Phys.*, 2013, **15**, 11236-11247.
67. G. Ramos-Sanchez and P. B. Balbuena, *Phys. Chem. Chem. Phys.*, 2013, **15**, 11950-11959.
68. G. Ramos-Sánchez and P. B. Balbuena, *J. Electroanal. Chem.*, 2014, **716**, 23-30.
69. E. Gracia-Espino, X. Jia and T. Wågberg, *J. Phys. Chem. C*, 2014, **118**, 2804-2811.
70. A. Nie, J. Wu, C. Zhou, S. Yao, C. Luo, R. C. Forrey and H. Cheng, *Int. J. Quantum Chem.*, 2007, **107**, 219-224.

Journal Name

RSCPublishing

ARTICLE

Table of Contents

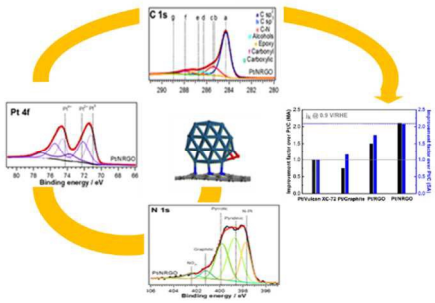

Confirmed by DFT, a significant amount of platinum atoms Pt are chemically bound to N of N-doped RGO.